Local transport in Joint European Tokamak edge-localized, high-confinement mode plasmas with H, D, DT, and T isotopes

R. V. Budny,[a] D. R. Ernst, T. S. Hahm, and D. C. McCune
Princeton Plasma Physics Laboratory, Princeton University, P. O. Box 451, Princeton, New Jersey 08543

J. P. Christiansen,[b] J. G. Cordey, C. G. Gowers, K. Guenther, N. Hawkes, O. N. Jarvis, P. M. Stubberfield, and K.-D. Zastrow
Culham Laboratory (UKAEA/Euratom) OX14 3DB, United Kingdom

L. D. Horton
MPI für Plasmaphysik, Boltzmannstrasse 2, D-85748 Garching, Germany

G. Saibene, R. Sartori, and K. Thomsen
EFDA Close Support Unit, Garching, MPI für Plasmaphysik, Boltzmannstrasse 2, D-85748 Garching, Germany

M. G. von Hellermann
FOM Institute for Plasma Physics Rijnhuizen, 3430 BE Nieuwegein, The Netherlands

(Received 3 May 2000; accepted 28 August 2000)

The edge-localized, high-confinement mode regime is of interest for future Tokamak reactors since high performance has been sustained for long durations. Experiments in the Joint European Tokamak [M. Keilhacker *et al.*, Nuclear Fusion **39**, 209 (1999)] have studied this regime using scans with the toroidal field and plasma current varied together in H, D, DT, and T isotopes. The local energy transport in more than fifty of these plasmas is analyzed, and empirical scaling relations are derived for energy transport coefficients during quasi-steady state conditions using dimensionless parameters. Neither the Bohm nor gyro-Bohm expressions give the shapes of the profiles. The scalings with β and ν_* are in qualitative agreement with Ion Temperature Gradient theory. © *2000 American Institute of Physics.* [S1070-664X(00)02912-8]

I. INTRODUCTION

One of the main objectives of Joint European Tokamak (JET) experiments is to contribute to the physics and technology needed to design International Thermonuclear Experimental Reactor (ITER).[1] The H-mode (high confinement) with the Edge Localized Mode (ELM), studied in JET[2] and other tokamaks, is the favored regime for ITER, since it has obtained enhanced performance (relatively large energy confinement times) for long durations (many energy confinement times). Many of the experiments during the recent extensive campaign in JET with DT plasmas[3] were devoted to studying these ELMy H-mode plasmas. The physics results of use for ITER include the scaling of the power threshold for the transition from L-mode to H-mode and the scaling of the global thermal energy confinement time, τ_E.[4]

Large extrapolations of the energy confinement times are necessary to go from present experiments to those needed to obtain high fusion yield in ITER. In order to increase confidence in the large extrapolations, dimensionless scaling arguments have been used to express $\langle\omega_c\rangle\tau_E$ as a unique, but unknown function of dimensionless parameters.[5] The thermal energy confinement time is normalized using the gyrofrequency of the hydrogenic ions, $\omega_c = eB/(m_{\rm H}A)$, with B the toroidal magnetic field, and A the profile of the isotopic mass of the thermal hydrogenic ions, defined in the Appendix. Here $\langle\cdots\rangle$ indicates a volume average.

A simple form for the unknown function is a product such as:

$$\langle\omega_c\rangle\tau_E \propto \langle\rho_*\rangle^{-a}\langle\beta\rangle^{-b}\langle\nu_*\rangle^{-c}\langle A\rangle^{-d}. \tag{1}$$

Here ρ_* is the ion-gyroradius normalized by a scale length, β is the normalized thermal pressure, and ν_* is the normalized ion collisionality. The plasma minor radius, a, is generally used for the normalizing scale length.

The values for the volume averages are often approximated using the total electron number, N_e and the total thermal energy, $W_{\rm th}$, i.e., $\langle\rho_*\rangle \propto \sqrt{AW_{\rm th}/(N_eB)}$, $\langle\beta\rangle \propto W_{\rm th}/B^2$, and $\langle\nu_*\rangle \propto N_e^3/W_{\rm th}^2$.

The form of Eq. (1) assumes the Kadomtsev constraint[6] that the Debye scale is irrelevant. Also it uses the convenient, but not theoretically justified assumption that the dimensionless parameters enter as a product of powers. Additional dimensionless parameters could be expected to be significant. One example is the ratio T_i/T_e. Equation (1) is generally used for ELMy H-mode plasmas in which $T_i \approx T_e$. We discuss deviations from $T_i = T_e$ below. Strictly, Eq. (1) is valid only if all other dimensional parameters, apart from those in Eq. (1) are held constant.

This dimensionless scaling approach has had success in fitting the results for $\langle\omega_c\rangle\tau_E$ of a large set of ELM-free and ELMy H-mode discharges.[7] Typically regression analysis is

[a]Electronic mail: budny@princeton.edu
[b]Present address: Euratom/UKAEA Fusion Association, Culham Science Center, Abingdon OX 14 3EA, United Kingdom.

TABLE I. Fit parameters for $\langle \omega_c \rangle \tau_E$ in Eq. (1).[a]

Dimensionless parameter	$\langle \rho_* \rangle$	$\langle \beta \rangle$	$\langle \nu_* \rangle$	$\langle A \rangle$
Fit values	A	B	c	d
Many Tokamaks (Ref. 7)	$+2.88$	$+0.68$	$+0.09$	-1.03
JET dataset	$+2.27 \pm 0.29$	-0.18 ± 0.27	$+0.05 \pm 0.11$	-0.62 ± 0.13

[a] $\langle \omega_c \rangle \tau_E \propto \langle \rho_* \rangle^{-a} \langle \beta \rangle^{-b} \langle \nu_* \rangle^{-c} \langle A \rangle^{-d}$.

applied to ''Engineering'' parameters such as the heating power, major radius R, minor radius a, and plasma current I_p. Then these scalings in engineering parameters are converted to scalings in the dimensionless parameters. The exponents in Eq. (1) from a regression analysis of ELMy plasmas in many tokamaks[7] are shown in Table I. A previous comparison (Ref. 7) of the JET ELMy results with the many-tokamak results indicated that JET has a much weaker scaling in $\langle A \rangle$, with $\langle \omega_c \rangle \tau_E \propto \langle A \rangle^{0.16}$.

Although our database, discussed below, is not optimized for studying global scaling, we performed regression to find the powers in Eq. (1). The scaling has smaller magnitudes for the powers than the many-tokamak result, but with a larger scaling in $\langle A \rangle$ than that in Ref. 7. The definition of τ_E and other parameters used here are given in the Appendix. Our result for $\langle \omega_c \rangle \tau_E$ is also shown in Table I. Large relative errors on our fit, calculated using the standard Analysis of Variation (ANOVA) expression,[8] are indicated. The results from our local transport analysis over a restricted range of radii given below also disagree with these global confinement scalings.

Several complications could explain these differences. JET results suggest a separate scaling for the core and pedestal. An example of such a fit, given in Ref. 9, is

$$\langle \omega_c \rangle \tau_E \propto \langle \rho_* \rangle^{-3} (1 + c \langle \rho_* \rangle^2 / \langle \beta_n \rangle^2), \tag{2}$$

where β_n is defined in Eq. (A8). This has the scaling of a gyro-Bohm core and Bohm pedestal. Also there are ambiguities in the volume averaging, especially for ν_*, whose profile has relatively large values near the axis and edge. Other possible causes of these disagreements are given in the discussion section.

The exponents of $\langle \rho_* \rangle$ in Table I are between -2 and -3, the values corresponding to Bohm and gyro-Bohm scaling respectively. Since ITER will require a large extrapolation to lower values of ρ_* compared with the values in JET, the scaling of $\langle \omega_c \rangle \tau_E$ with ρ_* is crucial. To understand confinement better, and to test theories, we also need to know the local confinement.

A series of experiments were conducted in JET to study the scaling of ELMy H-mode plasmas. This paper reports on the local transport analysis of about 50 of these plasmas. We show that although the transport coefficients do not have the shapes given by the Bohm or gyro-Bohm dependencies, they can be fitted over much of the plasma radius using local dimensionless parameters in analogy with Eq. (1). Preliminary results for the scaling of the transport coefficients at the half-radius were reported in a previous paper.[10] This paper extends that study in several ways: (1) A larger number of discharges are studied, and (2) transport over a wide range of radii are included.

Section II summarizes the various types of H-mode experiments in JET. Section III describes the measurements used, the TRANSP analysis code, and discusses the accuracy of the TRANSP results. The accuracy needs to be established since TRANSP results, such as for A and the transport coefficients, are used in the later analysis. Examples of the TRANSP simulations of the time evolution of the stored energy and the neutron emission rate are given. Section IV discusses results for transport coefficients. Section V describes the database of profile results at a typical quasi-steady time from each plasma. Ranges of parameters and accuracy of the simulations across the dataset are discussed. Section VI gives results from the regression analysis of an empirical fit for transport coefficients in terms of local dimensionless parameters. There is a trend for reduced transport with increasing β, which is consistent with a new ion temperature gradient (ITG) simulation. The increase in transport with collisionality is in qualitative agreement with the theory of collisional damping of zonal flows. In Sec. VII we briefly discuss implications for ITER. Section VIII discusses the results. The Appendix defines some of the expressions we use.

II. EXPERIMENTS

H-mode plasmas in JET can be classed as Hot-ion, ELM-free, or ELMy. Low target densities and sufficient heating powers produce Hot-ion H-modes with $T_i \gg T_e$. Higher target densities and/or lower heating powers produce the ELMy H-modes with $T_i \simeq T_e$. Generally the ELM-free plasmas evolve into ELMy plasmas during the pulse. The JET experiments to study these ELMy plasmas can be grouped into three classes:

(1) $L \rightarrow H$ power threshold studies. Experiments have investigated the dependence of the heating power threshold on A and B. The threshold has a strong dependence on A. In experiments in which the heating power is near the threshold, the ELM frequency decreases as the power is increased.[11] These ELMs are classified as Type III transition ELMs. The confinement in these is lower than that of discharges displaying the standard Type I ELMs, common in class (2);
(2) ρ_* scaling. In these experiments, ρ_* is varied by varying either A, B, power, or the density;
(3) identity experiments. These experiments constructed plasmas that are dimensionally identical to plasmas

formed in the ASDEX-Upgrade, DIII-D, and Alcator C-Mod tokamaks.[12] The goal of these studies is to check the dimensional scaling.

This paper focuses on the class (2), ρ_* plasmas. All of the plasmas were formed using the Mk-IIa divertor configuration.[13] We exclude plasmas formed with other divertor configurations since those have different characteristics.

III. DATA AND ANALYSIS

We used the TRANSP plasma analysis code[14] to analyze more than 50 of the JET ELMy H-mode discharges. A discussion of earlier uses of TRANSP to analyze JET plasmas is contained in Ref. 15. TRANSP is an interpretative code, making maximal use of measurements and minimal assumptions. All the JET plasmas used in this study have measured profiles for T_i, $Z_{\rm eff}$, and the toroidal rotation rate, $\omega_{\rm tor}$. These profiles were measured during the neutral beam injection (NBI) phase using charge-exchange spectroscopy.[16] For some of the plasmas, we extended the T_i and $\omega_{\rm tor}$ data out towards the edge using measurements from an edge spectroscopy system.[17]

We give examples of measured profiles for the DT plasma 42 982 with record fusion energy yield, $W_{\rm DT}=22$ MJ (Ref. 2) since this plasma is especially interesting as an ITER prototype. Waveforms, in Fig. 1, show that relatively high performance was sustained for more than four seconds. The ratio of fusion power to auxiliary heating power was $Q_{\rm DT}=0.18$, and the ratio of thermonuclear fusion power to auxiliary heating power was $Q_{\rm DT}^{tn}=0.07$.

Measured profiles are shown in Figs. 2 and 3. Charge-exchange spectroscopy profiles are shown in Fig. 2. The T_e profiles used are those measured by the Light Detection and Ranging (LIDAR) system.[18] Generally plasmas with B greater than about 2 T have T_e profiles measured by electron cyclotron emission as well, but since we include plasmas with B as low as 1 T in this study, we used the 5 Hz LIDAR measurements for all the plasmas to avoid systematic differences between the two measurement techniques. An example of measured T_e and n_e profiles are shown in Fig. 3. For n_e we use profiles synthesized from the LIDAR and interferometry measurements.[19] These profiles are normalized in shape by the LIDAR profiles.

TRANSP computes transport coefficients by comparing calculated fluxes with gradients of plasma profiles. Typically TRANSP models profiles using 20 zones equally spaced in the variable $x\equiv\sqrt{\text{normalized toroidal flux}}$ which is approximately equal to the normalized minor radius of the flux surface, r/a. Although TRANSP has recently been upgraded with the option to model 50 zones, the 20 zone option is adequate for this study.

In order to get relatively smooth transport coefficients from gradients, and to average over channel-to-channel systematic variations, we smoothed these measured profiles in the radial variable with a width of $x\leqslant 0.15$. We also smoothed the profiles in time with a 150–300 ms averaging window to average through sawteeth and ELMs.

The total hydrogenic influx from the wall and scrape off region, $S_{\rm hyd}$, is estimated from one of the measured H_α emission waveforms. Particle confinement times such as τ_e and τ_i are computed from the radial particle fluxes such as of the electrons, Γ_e and thermal hydrogenic ions, $\Gamma_{\rm hyd}$. The profile of $\Gamma_{\rm hyd}$ is well determined numerically by the measured n_e, $Z_{\rm eff}$, and computed particle sources, but the relative Γ_H, Γ_D, and Γ_T profiles need an additional constraint. Such a constraint was developed for modeling Tokamak Fusion Test Reactor (TFTR) supershots, and is also successful in modeling the JET plasmas, and is used here. An explicit diffusivity and relative pinch velocities are assumed for the hydrogenic species. This relative pinch velocity is assumed to be proportional to the inverse of the isotopic mass. Justification is indicated simply by the ability to simulate the measured total neutron emission rate as well as the chordal 14 MeV neutron emission profiles, as shown below.

The computed particle confinement times are in the ranges, $\tau_e/\tau_i\simeq 1.1$–1.5 and $\tau_i/\tau_E\simeq 0.5$–1.9. The relative fractions of H, D, and T in $S_{\rm hyd}$ are adjusted in the TRANSP input sets to get approximate agreement with the measured emission rates. These fitted fractions are in rough agreement with the species fractions measured in the edge and scrape off. For instance, the T fraction depends on the fraction of T in the NBI in the pulse and recent previous pulses. The fitted fraction is typically a few per cent in plasmas without T-NBI.

Examples of TRANSP results for the plasma with the record $W_{\rm DT}$ are shown in Figs. 4 and 5. The measured and calculated stored energies and the neutron emission rates are shown in Fig. 4. The 14 MeV neutron emission rate profiles are also measured.[20] A comparison of the TRANSP simulation and measurement is shown in Fig. 5. The sensitivity of the simulations to measurement uncertainties is indicated in the figures.

IV. TRANSPORT RESULTS

Several different transport coefficients are often used to describe measurements. Definitions are given in the Appendix. Generally χ_i and χ_e are defined by subtracting the ion and electron particle fluxes. Since there is some uncertainty in the calculation of the particle convection flux, we consider also $\chi_{\rm itot}$ defined to include both the convective and conductive transport, defined in Eq. (A3), and $\chi_{\rm eff}$ defined in Eq. (A4). The convection is calculated to be relatively small except near the edge, so $\chi_{i\rm tot}\simeq\chi_i$.

For the ELMy plasmas, $\chi_{\rm eff}$ is determined more accurately than either χ_i or χ_e separately. It is difficult to resolve χ_i and χ_e when $T_i\approx T_e$, as is typical for the plasmas studied here. Only global, not local measurements of the radiation emission profiles are available for the plasmas studied in this paper; this lack of more detailed information increases the uncertainty in determining χ_e. Typically, the TRANSP modeling gives χ_e roughly one-half χ_i near the mid-radius ($x\equiv 0.5$).

An example of $\chi_{\rm eff}$ for the $W_{\rm DT}=22$ MJ plasma is shown in Fig. 6. This figure shows the variability typically seen in JET ELMy plasmas. The results near the center are choppy due to sawteeth effects and the relatively flat profiles having

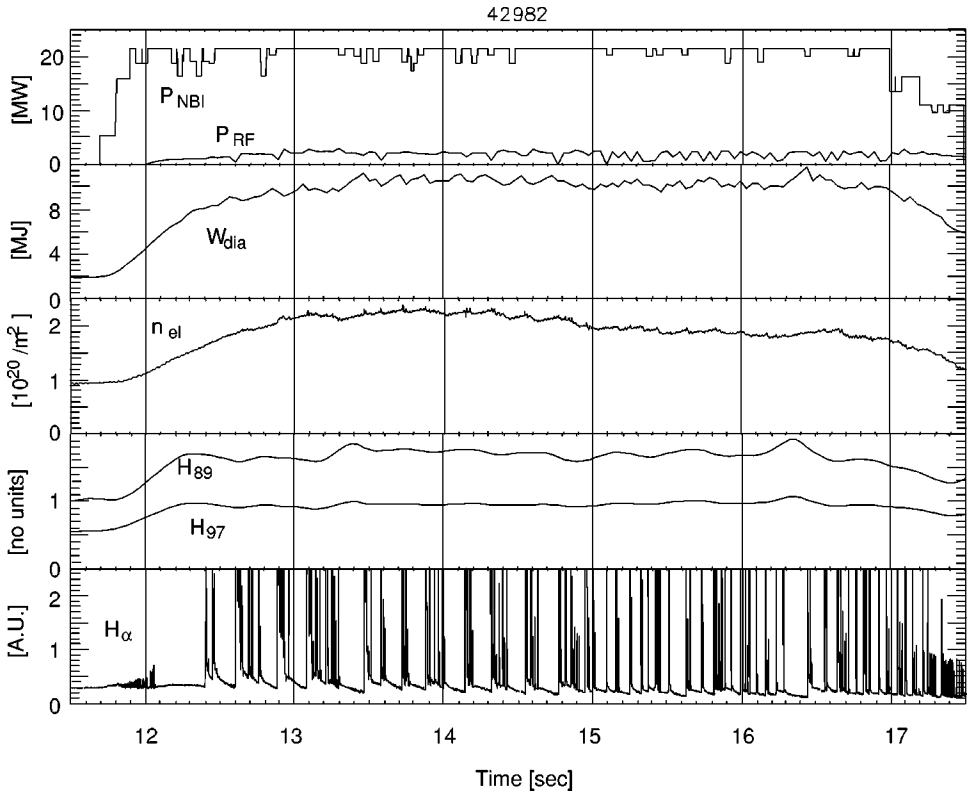

FIG. 1. Waveforms for the JET ELMy plasma with $W_{DT}=22$ MJ. The steady-state NBI consisted of 11 MW T-NBI and 10.6 MW D-NBI. The plasma current was 3.8 MA and the toroidal field was 4 T. β_n reached 1.3 and n_e reached 60 percent of the Greenwald limit. The ratios of the global energy confinement time and the ITER-89 and ITER-97 values are shown. The transition to H-mode occurs just before 12 s. The ELMy phase starts around 12.4 s, and continues past 17 s when the NBI power ramp down started. The analysis time selected here is 14.7 s, just before a sawtooth crash at 14.77 s.

near-zero gradients. The results near the edge are uncertain due to uncertainties in the convection, which is largest in the edge due to neutral influx from the scrape off region. The profiles are relatively smooth and constant in time near the mid-radius, and so we restrict our attention to the region $0.3<x<0.7$. χ_{eff} is compared with other transport coefficients in Fig. 7. The Bohm, gyro-Bohm, neoclassical, and empirical fit values are given for reference, and are discussed below.

V. DATABASE FOR REGRESSION ANALYSIS

A profile database was constructed from the TRANSP output at one relatively quiescent time during the auxiliary heating phase in each pulse. The plasmas in the database were selected to have an approximately constant ratio of B/I_p with B [T] and I_p [MA] varied between 1 and 4. The safety factor at the boundary, q_1, was restricted to the range 3.8–4.2. The NBI power ranged between 4 and 22 MW. Some of the plasmas had ion cyclotron resonance heating (ICRH), but we restricted the dataset to those with ICRH power less than 20% of the neutral beam power to minimize effects of the uncertainties modeling the ICRH power deposition. The range of T_i/T_e within the region $0.3<x<0.7$ is $0.7<T_i/T_e<1.3$.

Since the Type I and III ELMy phases have different confinement, we eliminated those identified as Type III. For some of the plasmas, especially those with H-NBI, it is difficult to determine if the ELM phase is Type I or III. Both Type III and transition ELMs have relatively high ELM frequencies, so we eliminated plasmas with ELM frequency greater than 150 Hz. Our results are not sensitive to the value used for this cutoff.

The profiles of the isotopic mass of the thermal hydrogenic species (omitting fast NBI and ICRH ions) A, defined in the Appendix Eq. (A5), ranged from approximately 1–3. Values of the Troyon-normalized thermal β_n, defined in Eq. (A8) ranged between 0.6 and 2.3, and the central values of the Mach number of the measured carbon toroidal rotation velocity, $\mathcal{M}_c$ ranged from 0.7 to 1.8. The values computed for the hydrogenic Mach number, $\mathcal{M}_h$ are reduced by two effects: The hydrogenic T_i is slightly less[21] than the measured carbon T_i and the hydrogenic A is used instead of 6 for carbon. The central values of $\mathcal{M}_h$ ranged from 0.05 to 0.8, and the values at the half-radius ranged from 0.2 to 0.5, as shown in Fig. 8. The database shows a tendency for these values to increase with A, but to be relatively constant at constant I_p.

One of the important parameters that needs to be computed is the energy of the fast ion species. Some of the heating power can heat the fast ions and some of the heat is lost by the fast ions. Only the thermal energy and energy losses are used for τ_E, Eq. (A1) and the transport coefficients. The fraction of the total energy carried by the fast ions is typically 5–20 percent, but is as high as 45 percent for several plasmas in the database.

The degree of accuracy of the TRANSP modeling across

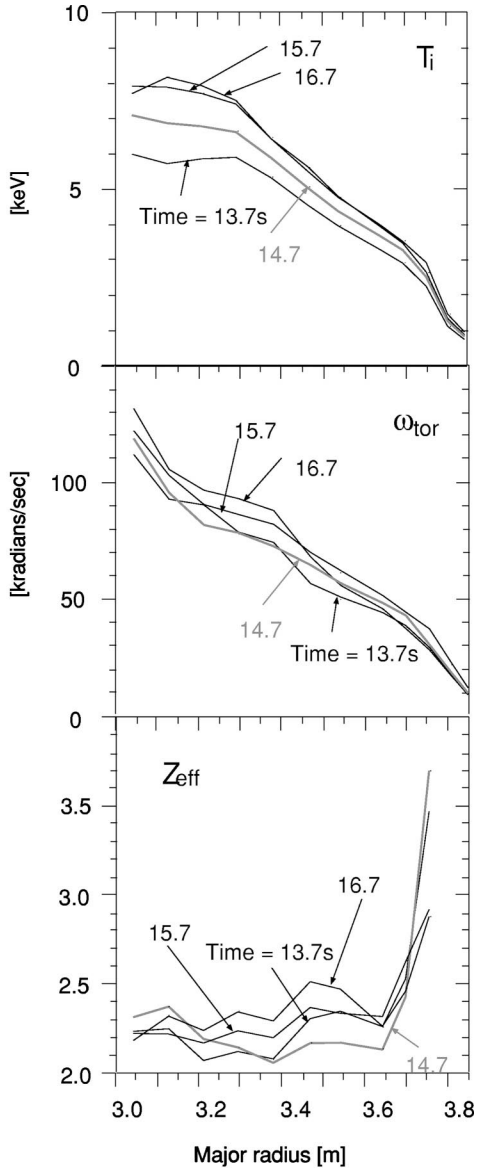

FIG. 2. T_i, toroidal rotation frequency, ω_{tor}, and Z_{eff} measured by charge-exchange spectroscopy. The measurements from the central charge exchange system extend to a major radius of 3.75 m. The measurements of T_i and ω_{tor} have been combined with the measurements from the edge charge exchange system. The two systems are in approximate agreement at 3.75 m.

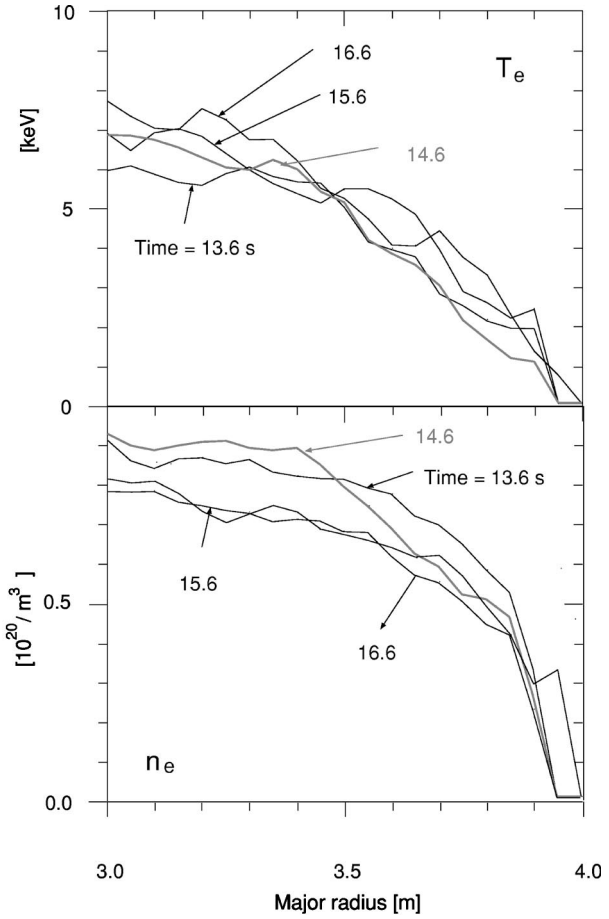

FIG. 3. Electron temperature and density measured by LIDAR. These measurements indicate that the top of the pedestal occurs near $R=3.85$ m. The charge-exchange measurements shown in Fig. 2 and the electron-cyclotron-emission measurements indicate that the pedestal occurs near $R=3.75$ m.

the data base is indicated in Fig. 9, where the ratios of the TRANSP simulations and measurements are plotted. Most of the simulations have total energy within ten percent of the measured values, and total neutron emission rates within thirty percent on the measured values. In the case of the H-NBI plasmas, there is considerable uncertainty simulating their neutron emission rates due to the extreme sensitivity on the trace amounts of D and T entering these plasmas from the walls. Likewise, the neutron emission rates from the D-only plasmas depends sensitively on the T influx from the walls.

There is a systematic trend for TRANSP to underpredict the measured energy at low $\langle\beta\rangle$ and to overpredict at high $\langle\beta\rangle$. This is shown in Fig. 10. The plasmas with the highest $\langle\beta\rangle$ have the lowest I_p and have mode activity such as fishbones or toroidal Alfvénic eigenmode (TAE). Such mode activity probably causes anomalous loss of confinement of the fast beam ions. Anomalous loss is generally not modeled in TRANSP, explaining at least some the overestimation in $\langle\beta\rangle$.[22] The reason for TRANSP underestimating the stored energy at low $\langle\beta\rangle$ is not understood. To compensate for this, the regression results for the transport coefficients are scaled by the ratio of the TRANSP to magnetically measured energy values shown in Fig. 10. Without this renormalization, the empirical fit values change of order 5 percent.

Ranges of derived physics parameters are shown in Figs. 8, 11–13. The ranges of ρ_* and A at the mid-radius are shown in Fig. 11. The values expected for ITER-FDA are shown for comparison. Note that I_p is relatively low for the H plasmas, as seen in Fig. 8. The main reason that the I_p is low for the H plasmas is that the available NBI heating power is much lower with H injection, only 10 MW as opposed to 20 MW with the D and DT injection. The power threshold for the H-mode decreases with isotopic mass and increases with B. Also the central Z_{eff} is relatively high, and tends to increase with A, as shown in Fig. 12.

There are other covariances among the parameters in the database, as have been described previously.[10,23] For in-

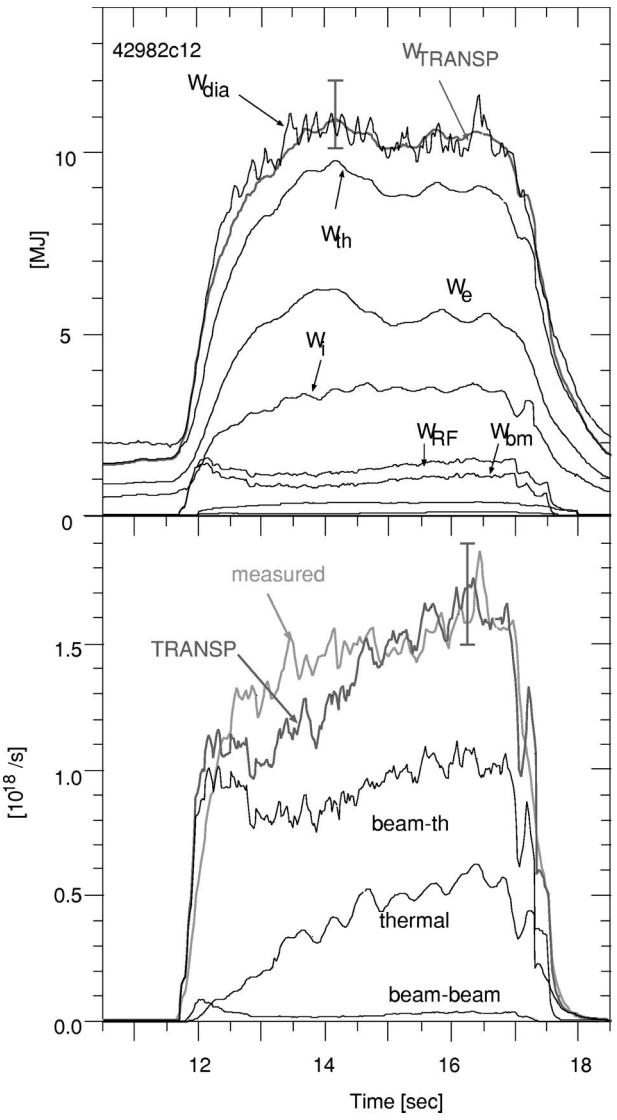

FIG. 4. Comparisons of the measured and calculated stored energy and neutron emission rates. The diamagnetically measured energy W_{dia} agrees well with the TRANSP simulation W_{TRANSP} during the NBI phase. W_{TRANSP} includes the transverse component of the fast ion energy from the NBI and ICRH, multiplied by 3/2 and added to the thermal plasma energy. The TRANSP simulated neutron emission rate is dominated by the DT rate, which is the sum of the beam–beam, beam–thermal, and thermonuclear rates. The ''error'' bars on the TRANSP simulations indicate the envelopes of separate TRANSP runs in which one of the inputs for T_i, T_e, n_e, ω_{tor}, or Z_{eff} was varied up or down by 10 percent. The baseline TRANSP run uses the unaltered measurements. The upper and lower bounds on W_{TRANSP} result from $(1\pm0.1)n_e$. The upper and lower bounds on the TRANSP neutron emission rate are given by both $(1\pm0.1)T_i$ and $(1\pm0.1)Z_{\mathrm{eff}}$.

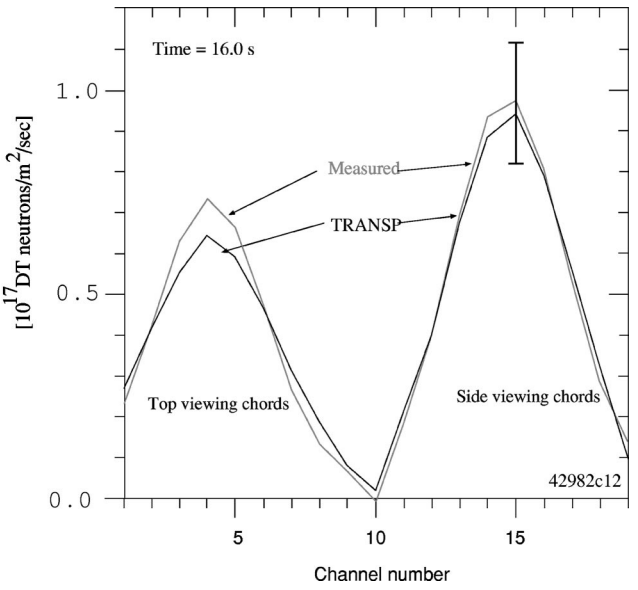

FIG. 5. The measured and TRANSP-simulated chordal 14 MeV neutron emission rates. Chords 1–9 are from the top view and chords 10–19 are from the midplane view. The ''error'' bar on the TRANSP total indicates the envelope of simulations of ten additional TRANSP runs for which one of the inputs was varied up or down by 10 percent, as in Fig. 4. The upper and lower bounds of the envelope results from $(1\pm0.1)T_i$.

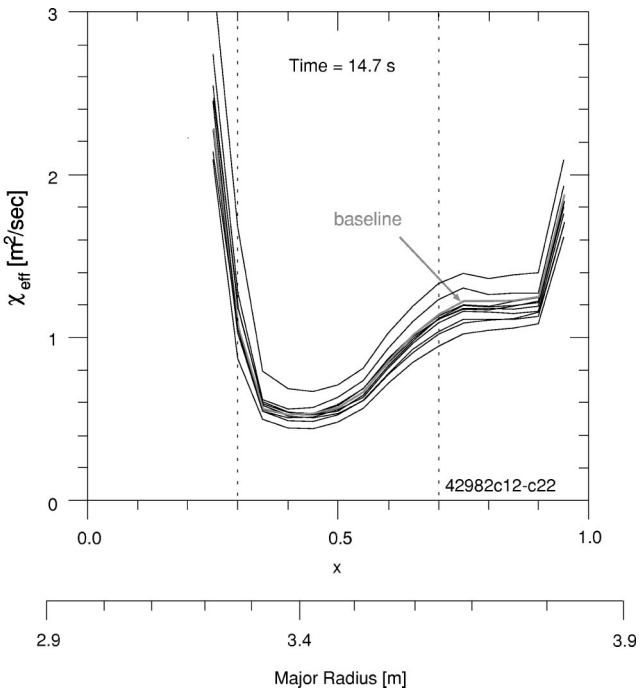

FIG. 6. Profiles of χ_{eff} versus the radial index x. defined as $x \equiv \sqrt{\text{normalized toroidal flux}}$. Typically large variations in time and radius are seen near the center, where sawtooth effects are important, and near the edge, where ELMs are important, and uncertainties of neutral densities play a role. Ten TRANSP runs are overlaid with the baseline run to show the range of simulations gotten by varying inputs for T_i, T_e, n_e, ω_{tor}, or Z_{eff} up or down by 10 percent. The lower and upper profiles result from $(1\pm0.1)n_e$. The region between the dashed lines at $x=0.3$ and $x=0.7$ is the region used for the regression analysis. The corresponding values of major radius are indicated. The top of the pedestal is near $R=3.75$–3.85 m.

stance, the central electron density, $n_e(0)$ is larger at higher A and I_p, and the peaking, $n_e(0)/\langle n_e\rangle$, decreases systematically with A. These are shown in Fig. 13. Thus the electron density profiles in H plasmas are relatively peaked and those of T plasmas are flat or even hollow. Also, when $T_i \approx T_e$, $\beta \propto n_e \rho_i^2/A$. At fixed r/R, ν_* and β are related, but their different r/R dependences allow us to separate them in the regression. Ranges of plasma parameters throughout the database are summarized in Table II.

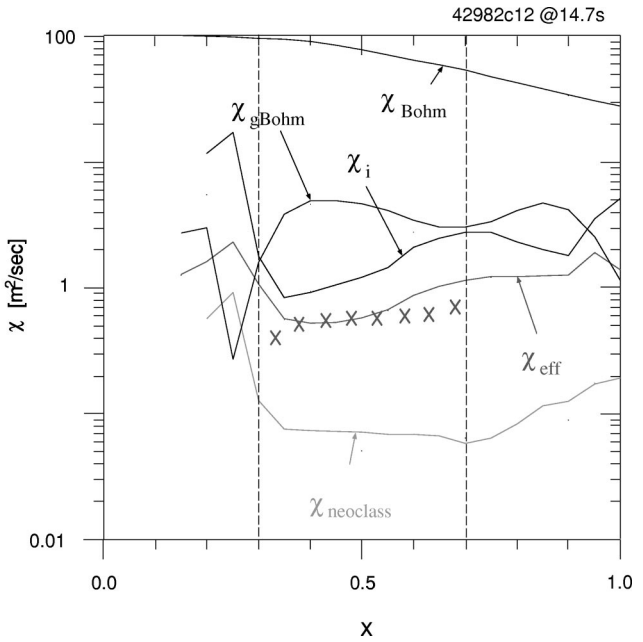

FIG. 7. Transport coefficients χ_i and χ_{eff} compared with χ_{Bohm}, $\chi_{g\text{Bohm}}$, χ_{neoclass} and the empirical fit to χ_{eff}. The empirical fit, Eq. (3), given by x, is derived from the whole data set, restricted to $0.3<x<0.7$, and applied to this plasma.

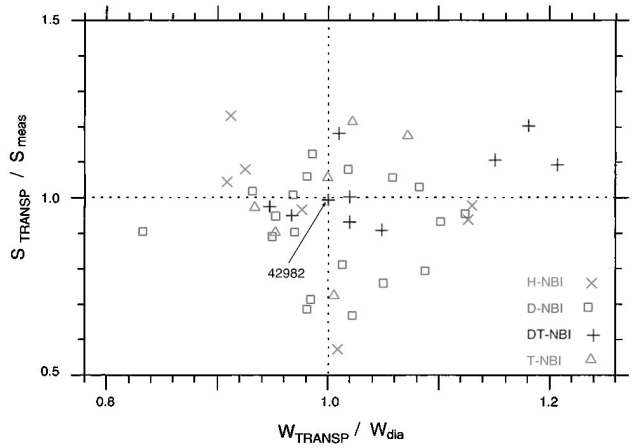

FIG. 9. Range of values of the ratios of the TRANSP-computed and measured total neutron emission rates and stored energy. Agreement between the measurements and simulations occur at the point (1.0,1.0). The H-NBI pulses have very low neutron rates, and the TRANSP modeling depends sensitively on the small amounts of D and T in the plasmas.

VI. TRANSPORT MODELING

A. Dimensionally correct scaling

Early theory suggested that the local transport coefficient profiles such as χ_i should be proportional to either the Bohm or gyro-Bohm expressions. We define the Bohm transport coefficient as $\chi_{\text{Bohm}} \equiv T_e/(16B)$ using the historical factor 16. Generally the gyro-Bohm transport coefficient is defined as $\chi_{g\text{Bohm}} \equiv T_i \rho_* / B$. Here and below, the ion temperature scale length, $L_{\text{Ti}} \equiv -T_i/(\partial T_i/\partial r)$ is used for the normalization for ρ_*. Alternative scale lengths, such as $L_{ne} \equiv -n_e/(\partial n_e/\partial r)$ are also important in ITG models, but L_{ne} tends to be larger than L_{Ti} for the plasmas we consider, and the smaller scale length is expected to be more relevant for determining the dynamics. As noted above, some of the T-NBI plasmas have hollow n_e.

For comparison, the profiles of χ_{Bohm}, $\chi_{g\text{Bohm}}$, and the neoclassical transport,[24] χ_{neoclass} were shown in Fig. 7. As can be seen, these simple theoretical profiles are very different from the measured profiles. The plots of the ratios $\chi_i/\chi_{g\text{Bohm}}$ and $\chi_i/\chi_{\text{Bohm}}$ versus radius show a marked increase as x increases beyond $x \simeq 0.3$. Typically $\chi_i/\chi_{g\text{Bohm}}$ increases by about a factor of ten between $x \simeq 0.3$ and 0.7.

Regression analysis leading to expressions such as Eq. (1) show a scaling in ρ_* between Bohm and gyro-Bohm. The measured transport at a fixed radius might still scale, say as gyro-Bohm in ρ_*. This could be tested by comparing plasmas where only ρ_* varied, say by varying A or B. Unfortunately the plasma profiles could not be held constant in the JET experiments. For instance, n_e tended to increase as either A or B increased. Even if pairs of discharges where only one dimensionless parameter changed cannot be found,

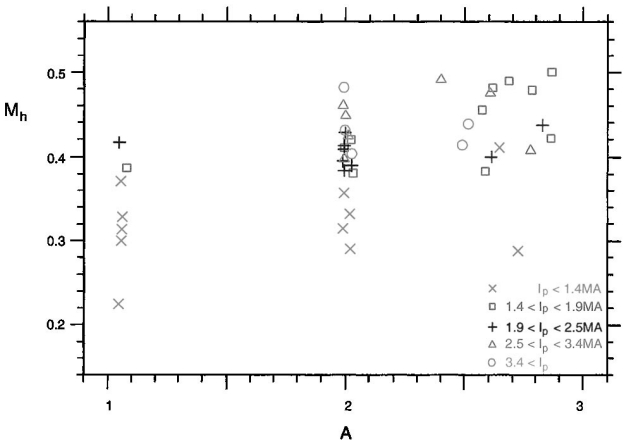

FIG. 8. Range of values of the hydrogenic-ion toroidal Mach number and A at the half-radius.

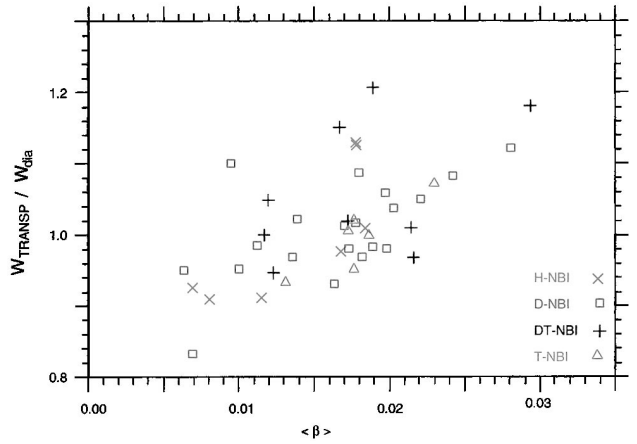

FIG. 10. Range of values of the ratios of the TRANSP-computed and measured stored energy versus $\langle\beta\rangle$. The pulses with highest $\langle\beta\rangle$ have fishbone or other MHD activity. Several plasmas with TAE are excluded from the regression.

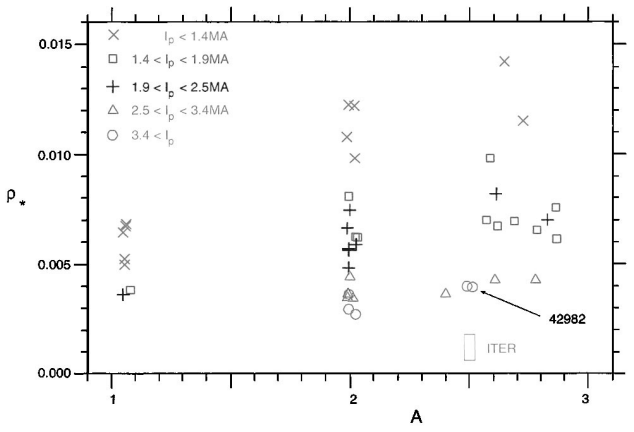

FIG. 11. Range of values in the database of the local ρ_* and A at the half-radius. The pulses are grouped into ranges of I_p. The values expected for ITER are in the range $\rho_* \approx 0.001-0.002$ and $A \approx 2.5$.

dimensionless scaling implies that a unique function of dimensionless parameters governs the transport. We assume this function has the form of a product of powers as in Eq. (1).

We studied the scaling of the dimensionless ratios of transport coefficients normalized by the product $\omega_c L_{\mathrm{Ti}}^2$, which has the dimensions for a conductivity [length^2/time]. We restricted the fit range of the toroidal flux index, $0.3<x<0.7$, to exclude the central region, where sawtooth effects cause periodic changes in plasma parameters, and the edge region, where ELMs cause periodic changes. This range includes eight of the twenty radial zones from the TRANSP-symmetrized data for each plasma.

The normalized χ_i can be fitted approximately over this range of x using the local values of the parameters in the right-hand-side of Eq. (1):

$$\chi_i/(\omega_c L_{\mathrm{Ti}}^2) \simeq f_{\mathrm{i}} \propto \rho_*^{+a'} \beta^{+b'} \nu_*^{+c'} A^{+d'}, \tag{3}$$

Regression gives the values of the powers and their statistical uncertainties given in Table III. The value of R^2 for the fit from the standard ANOVA expression, is 92 percent. Also the regression fits for f_{eff}, $f_{i\mathrm{tot}}$, etc., for χ_{eff}, $\chi_{i\mathrm{tot}}$, the cross-field toroidal momentum transport coefficient, χ_{mom}, and,

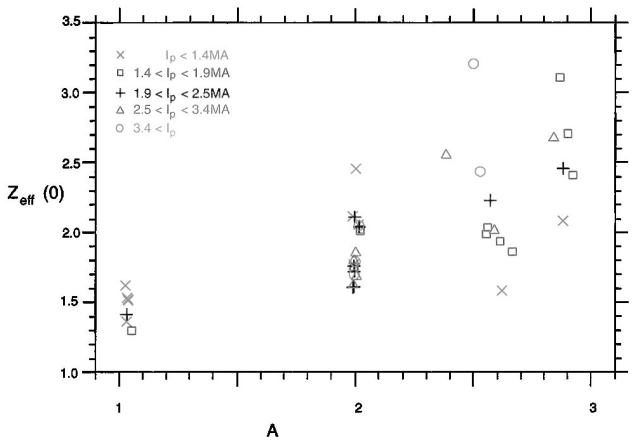

FIG. 12. Range of values of the central Z_{eff} and A.

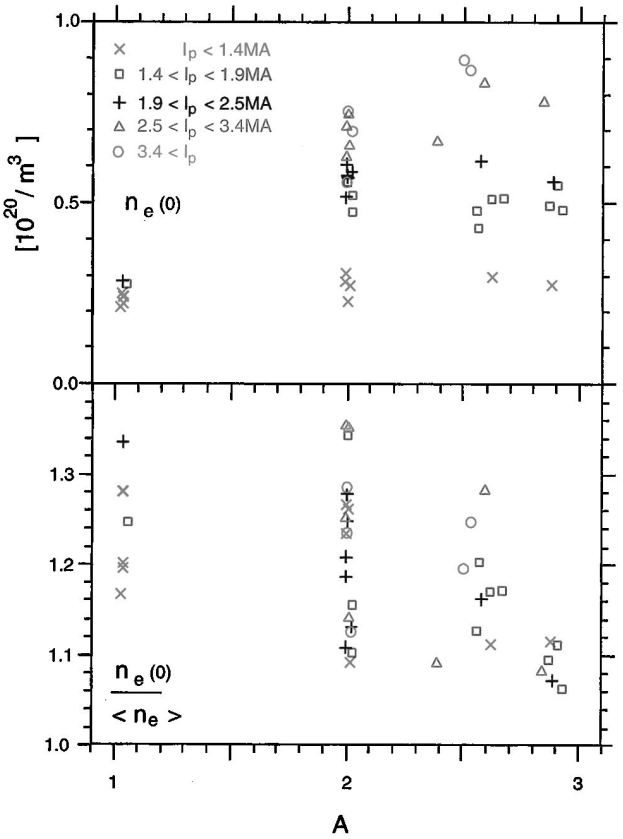

FIG. 13. Range of values of the central electron density and of the electron density peakedness, defined as the ratio of the central and volume-averaged electron density, and the central isotopic mass, A.

the effective electron particle transport, D_e, using the same fit range and normalization, are given in the table.

The explicit signs of the exponents in Eq. (3) are opposite to those in Eq. (1) since the profiles of the local τ_E and χ_{eff} are expected to scale roughly as inverses of each other. The global fits in Table I and our new results in Table III have similar values for ρ_*, and A, but not β, and ν_*. A plot

TABLE II. Ranges of parameters from the database for regression analysis.

Parameter	Range
R[m]	2.89–2.93
a[m]	0.89–0.93
I_p[MA]	0.90–4.0
q_1 (safety factor at boundary)	3.80–4.20
ε_1 (inverse aspect ratio at boundary)	0.305–0.324
κ_1 (elongation at boundary)	$\approx$1.63
δ_1 (triangularity at boundary)	$\approx$0.25
P_H[MW]	6.0–8.0
P_D[MW]	1.0–18.0
P_T[MW]	4.0–11.0
P_{ICRH}[MW]	0.5–2.5
$\langle \beta_{\mathrm{th}} \rangle$	0.005–0.030
β_n	0.6–2.3
$T_i(0), T_e(0)$[keV]	2.0–7.0
T_i/T_e	$\approx$0.7–1.3
$n_e(0)$[10^{20}/m^3]	0.2–0.9
$\overline{n_e}/n_{\mathrm{Greenwald}}$	0.28–0.78
A	1.0–3.0

TABLE III. Regression analysis results for the fits, $f_{\rm eff}$, etc. to the transport coefficients. The data for the effective thermal transfer coefficient, $\chi_{\rm eff}$, the thermal ion coefficient excluding convection, χ_i, and including convection, $\chi_{i\rm tot}$, the effective momentum transport, $\chi_{\rm mom}$, and the effective electron particle diffusion, D_e, are normalized by $(\omega_c L_{\rm Ti}^2)$ as in Eq. (3).[a]

Transport coefficient data	parameters: fit	constant k'	ρ_* a'	β b'	ν_* c'	A d'
$\chi_{\rm eff}/(\omega_c L_{\rm Ti}^2)$	$f_{\rm eff}$	4.85 ± 0.22	$+2.42\pm0.04$	-0.57 ± 0.05	$+0.54\pm0.03$	-0.94 ± 0.06
$\chi_i/(\omega_c L_{\rm Ti}^2)$	f_i	5.79 ± 0.22	$+2.19\pm0.05$	-0.75 ± 0.06	$+0.74\pm0.03$	-0.84 ± 0.06
$\chi_{i\rm tot}/(\omega_c L_{\rm Ti}^2)$	$f_{i\rm tot}$	6.44 ± 0.24	$+1.99\pm0.05$	-0.63 ± 0.06	$+0.71\pm0.04$	-1.06 ± 0.06
$\chi_{\rm mom}/(\omega_c L_{\rm Ti}^2)$	$f_{\rm mom}$	5.01 ± 0.29	$+2.55\pm0.06$	-0.53 ± 0.07	$+0.43\pm0.04$	-0.91 ± 0.08
$D_e/(\omega_c L_{\rm Ti}^2)$	f_e	4.89 ± 0.67	$+2.63\pm0.13$	-0.41 ± 0.16	$+0.23\pm0.09$	-1.37 ± 0.18

[a] $\chi/(\omega_c L_{\rm Ti}^2)=e^{k'}\rho_*^{a'}\beta^{b'}\nu_*^{c'}A^{d'}$, where the proportionality constant is written as a power of Euler's constant.

of $\chi_i/(\omega_c L_{\rm Ti}^2)$ versus $f_{\rm i}$ is shown in Fig. 14. The accuracy of the fits is best for $\chi_{\rm eff}$ and decreases descending down Table III. The inaccuracy and scatter for D_e is relatively large.

We tested the fits by constraining the dataset, holding one of the four dimensionless parameters approximately constant and performing regression on the remaining three parameters. The resulting scaling is approximately the same as that given in Table III.

The fits in Table III have the power a' between the Bohm value (2) and the gyro-Bohm value (3), which is more favorable for ITER-sized reactors. The data include large variations from a simple ρ_*^3 scaling expected for gyro-Bohm. This can be seen in Fig. 15, where the ratio $(\chi_i/(\omega_c L_{\rm Ti}^2))/\rho_*^3$ is plotted versus β. Even at fixed β a wide variation is seen, and the hydrogen plasmas tend to have higher values of $(\chi_i/(\omega_c L_{\rm Ti}^2))/\rho_*^3$ than those of the other isotopes. This ratio tends to decrease with β, but may be saturating at high β. This is discussed further below.

Since it is important to substantiate the decrease with β, we need to separate the dependences on β and ν_*. To do this we show that even if ν_* is approximately constant, the decrease is maintained. The dominant term in the regression is ρ_*, so we divide out the ρ_* dependence, using a power for ρ_* in the range gotten from regression, between the gyro-Bohm (3) and Bohm (2) values, i.e., $\rho_*^{2.35}$. Figure 16 shows $(\chi_i/(\omega_c L_{\rm Ti}^2))/\rho_*^{2.35}$ versus β with ν_* grouped in three ranges. The decrease with β is seen for each range of ν_*. Similarly, if the data are grouped by I_p, each group shows the trend to decrease with β. The data with the lowest I_p are high on the cluster in Fig. 16, and those with high I_p are low. Similarly, the ratio $(\chi_i/(\omega_c L_{\rm Ti}^2))/\rho_*^{2.35}$ shows a systematic decrease with A and an increase with ν_*.

The decrease of the fit Eq. (3) with increasing β is in qualitative agreement with a recent extension of gyrofluid simulation to include electromagnetic effects.[25,26] This theory predicts a decrease of heat flux as β increases up to a critical value. This decrease may be related to the reduction of the (non-linear) growth rate with β, and the increased coupling with Alfvénic fluctuations. The plot in Fig. 15 suggests a leveling-off at high β. The ITG simulations cited above indicate an increase in heat transport above a critical β, about half of the ideal magnetohydrodynamic (MHD) β limit in one case.

The fit Eq. (3) also indicates an increase with increasing ν_* since c' is positive. H-mode plasmas in DIII-D also show an increase in heat transport[27] with ν_*, $\chi_{\rm eff} \propto \chi_{\rm Bohm}\nu_*^{0.49\pm0.08}$. This range for the power for ν_* is within the range 0.48 ± 0.03 given in Table III. Many gyrofluid simulations, including early work[28] observe reduced transport with increasing zonal flows, which make the radial correlation length of the microturbulence smaller.[29,30] The zonal flows are damped by collisions, so increased collisionality should correlate with increased χ_i or $\chi_{\rm eff}$, as observed in recent gyrokinetic simulations.[31]

Our database is useful for testing results from gyrofluid and gyrokinetic simulations. For instance, global gyrokinetic simulations[32] in which ρ_* was varied by varying the simulation box size observe that the ratio of $\chi_{\rm eff}$ and $\chi_{g\rm Bohm}$ should saturate only at large values of $1/\rho_*$ ($>\simeq 200$). If $\chi_{\rm eff}$ is simply gyro-Bohm without corrections, this ratio should be unity. Figure 17 shows a plot of this ratio for a restricted range of x and $R/L_{\rm Ti}$. These is a suggestion of saturation at the highest values of $1/\rho_*$.

The measured values of χ_i for the plasma with record $W_{\rm DT}$ are compared with the fit in Fig. 7. The fit profile is shown in that figure as X's. The comparison shows that this plasma, at the time chosen, has $\chi_{\rm eff}$ slightly larger than average. Often the fit is in approximate agreement with measurements even outside the range $0.3<x<0.7$ where the fit was derived.

B. Additional dimensionless parameters

To increase the confidence in the fits, we looked for trends in the ratio of $\chi_i/(\omega_c L_{\rm Ti}^2)$ and the fit $f_{\rm i}$ with various parameters such as B, the electron density peaking factor, and the ELM frequency, normalized using ω_c. No clear trends with these are apparent, although the database does show trends for this ratio to decrease with the Mach number of the toroidal rotation, $\mathcal{M}_h$, and also with the ratio T_i/T_e. These cause some of the spread of the data around the fits, shown in Fig. 14. In Ref. 10, $\mathcal{M}_h$ was used as an additional dimensionless parameter for a power fit, generalizing Eq. (3). A strong dependence, approximately $\mathcal{M}_h^{-1}$, was found. Our enlarged database shows a similar, strong dependence when $\mathcal{M}_h$ is used as a fifth dimensionless parameter. Regression gives:

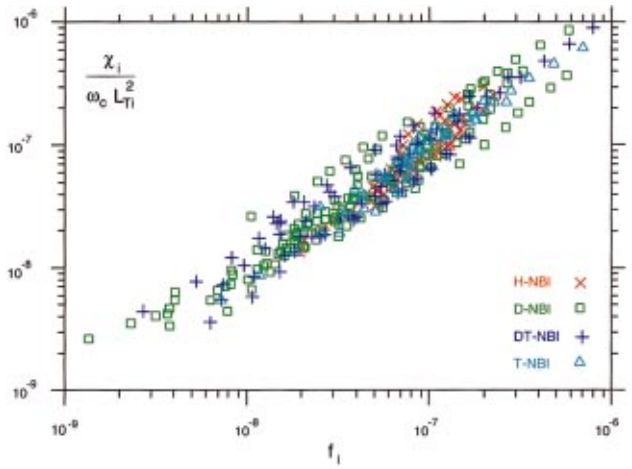

FIG. 14. (Color) Plot of the TRANSP-measured versus the fitted values of $\chi_i/(\omega_c L_{\mathrm{Ti}}^2)$, restricted to $0.3<x<0.7$. The pulses with H-, D-, DT-, and T-only NBI are indicated.

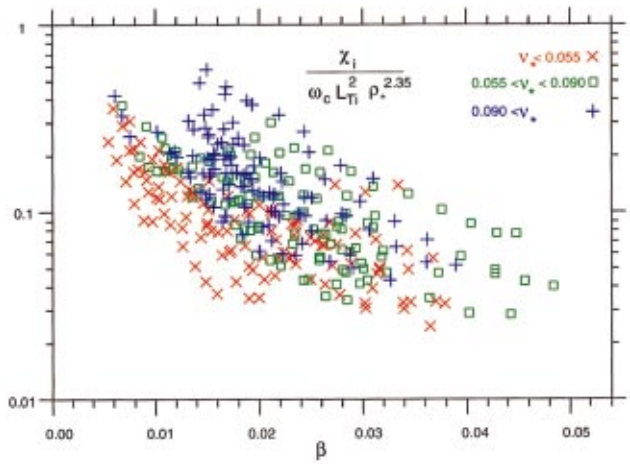

FIG. 16. (Color) Plot of the normalized $(\chi_i/(\omega_c L_{\mathrm{Ti}}^2))/\rho_*^{2.35}$ versus β with ν_* values divided into three ranges indicated. Each range shows a decrease with β. The dataset is restricted to $0.3<x<0.7$.

$$\chi_i/(\omega_c L_{\mathrm{Ti}}^2) \propto \rho_*^{+1.93\pm0.05}\beta^{-0.59\pm0.05}\nu_*^{+0.59\pm0.03} \times A^{-0.40\pm0.07}\mathcal{M}_h^{-1.2\pm0.12}. \quad (4)$$

Note that the ρ_* dependence has shifted even further towards the Bohm value, and the β power is weaker, as some of the β radial dependence is shifted to that of $\mathcal{M}_h$. There is a strong covariation of $\mathcal{M}_h$ with T_i, and a weak covariance with β. In fact, regression using $\mathcal{M}_h$ in place of β in Eq. (3) gives a fit nearly as good as that in Table III.

One disadvantage of using $\mathcal{M}_h$ as a power fit is that such a fit is not very useful for extrapolations to ITER which is expected to have a relatively small toroidal rotation, and values of $\mathcal{M}_h$ lower than JET ELMy plasmas by at least an order of magnitude.

We attempted to increase the relevancy of an empirical fit that incorporates toroidal rotation by including a correction to Eq. (3) which features a linear dependence on $\mathcal{M}_h$. A decrease of χ_i with $\mathcal{M}_h$ is expected in recent physics-based models[33] that indicate that microturbulence, and thus χ_i, is reduced by shear in the $E\times B$ rotation caused by the radial electric field, E_r. The equilibrium force balance indicates that for plasmas strongly rotating in the toroidal direction, the toroidal rotation is the dominant contribution to E_r, and $\mathcal{M}_h$ is a good indicator of the $E\times B$ shear effect. This effect is indicated in Ref. 34

$$\chi_i = \chi_0\left[1-\alpha\frac{|\omega_{\mathrm{E}\times\mathrm{B}}|}{\gamma_{\max}}\right], \quad (5)$$

where χ_0 is the prediction without sheared flow, α is a constant of order 1, $\gamma_{\max}$ is the maximum growth rate for the microturbulence, and $\omega_{\mathrm{E}\times\mathrm{B}}$ is the flow shearing rate.

$\omega_{\mathrm{E}\times\mathrm{B}}$ on the outer midplane is given[30] in terms of the radial electric field, E_r, by

$$\omega_{\mathrm{E}\times\mathrm{B}} = \left(\frac{R^2B_{\mathrm{Pol}}^2}{B}\right)\frac{\partial}{\partial\psi}\left(\frac{E_r}{RB_{\mathrm{Pol}}}\right) \simeq \left(\frac{RB_{\mathrm{Pol}}}{B}\right)\frac{\partial}{\partial R}\left(\frac{E_r}{RB_{\mathrm{Pol}}}\right). \quad (6)$$

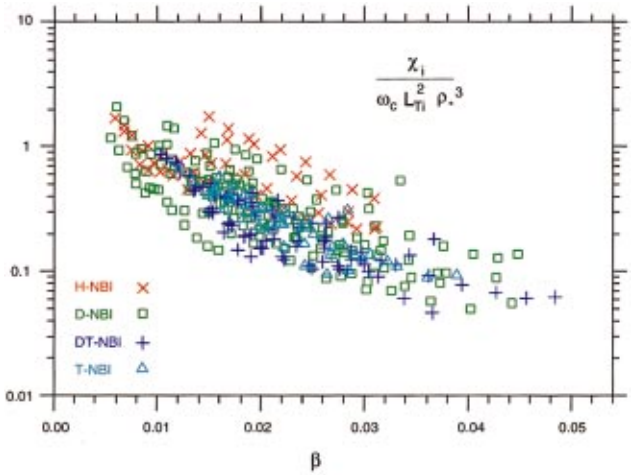

FIG. 15. (Color) Plot of the normalized $(\chi_i/(\omega_c L_{\mathrm{Ti}}^2))/\rho_*^3$ versus β showing a wide spread at constant β and a tendency to decrease with β. The dataset is restricted to $0.3<x<0.7$ and the isotope of the NBI is indicated.

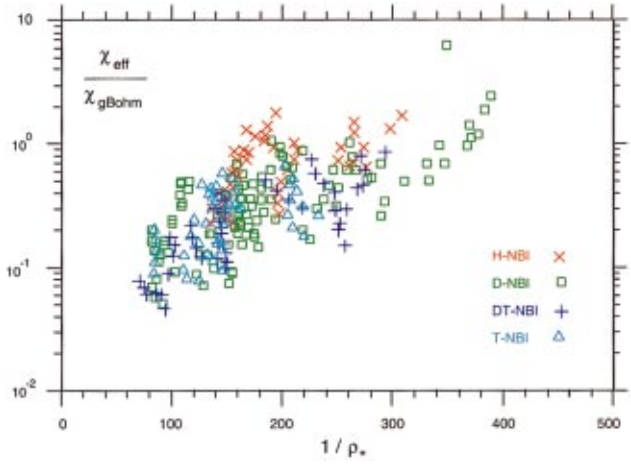

FIG. 17. (Color) Plot of $\chi_{\mathrm{eff}}/\chi_{g\mathrm{Bohm}}$ versus $1/\rho_*$. Global gyrokinetic simulations indicate that $\chi_{\mathrm{eff}}/\chi_{g\mathrm{Bohm}}$ should increase with $1/\rho_*$, and then saturate at large values of $1/\rho_* \geqslant\approx 200$. The range of the JET results is restricted to $0.3<x<0.7$ and $4<R/L_{\mathrm{Ti}}<6$.

E_r can be calculated from the equilibrium force balance for the carbon impurity

$$E_r = v_{\mathrm{Tor}} B_{\mathrm{Pol}} - v_{\mathrm{Pol}} B_{\mathrm{Tor}} + \frac{1}{Z_{\mathrm{imp}} e n_{\mathrm{imp}}} \nabla(p_{\mathrm{imp}}), \tag{7}$$

where n_{imp} and p_{imp} are the measured impurity density and pressure ($\propto n_{\mathrm{imp}} T_{\mathrm{imp}}$), and Z_{imp} is the charge of the impurity (6 here). B_{Pol} is calculated by TRANSP solving the poloidal field diffusion. v_{Pol} is calculated from neoclassical theory.[24,35] In the region $0.3<x<0.7$ of the JET ELMy plasmas, the gradient of the pressure term is relatively small, so the toroidal rotation term dominates if the poloidal rotation is of the order of the neoclassical value. In this case

$$\frac{E_r}{R B_{\mathrm{Pol}}} \approx \frac{v_{\mathrm{tor}}}{R} = \omega_{\mathrm{tor}}. \tag{8}$$

If the plasmas are far from marginal stability, the maximum growth rate is expected to scale on the order of $\gamma_{\max} \propto k_\theta \rho_i v_{\mathrm{th}} / \sqrt{R L_{\mathrm{Ti}}}$, so, at constant $k_\theta \rho_i$, the shearing term in Eq. (5) should scale as

$$\frac{\omega_{\mathrm{E}\times\mathrm{B}}}{\gamma_{\max}} \propto \frac{B_{\mathrm{Pol}}}{B} \frac{\sqrt{R L_{\mathrm{Ti}}}}{L_{\mathrm{tor}}} \mathcal{M}_h \approx \frac{\kappa \varepsilon}{q} \frac{\sqrt{R L_{\mathrm{Ti}}}}{L_{\mathrm{tor}}} \mathcal{M}_h, \tag{9}$$

where κ is the plasma elongation, ε is the local inverse aspect ratio, r/R, and L_{tor} is the scale length of the toroidal rotation.

We attempt to fit our results using

$$\chi_{\mathrm{eff}} / (\omega_c L_{\mathrm{Ti}}^2) \approx f_{\mathrm{eff}} \left[1 - c \frac{\kappa \varepsilon}{q} \frac{\sqrt{R L_{\mathrm{Ti}}}}{L_{\mathrm{tor}}} \mathcal{M}_h \right], \tag{10}$$

in the range $0.3<x<0.7$ with f_{eff} given in Table III. The ratio $(\chi_{\mathrm{eff}}/(\omega_c L_{\mathrm{Ti}}^2))/f_{\mathrm{eff}}$ does not show a clear trend, i.e., there is too much scatter to determine c. A similar null result is found for χ_i using f_{i}. Several mechanisms may explain this null result: (1) The value of $|\omega_{\mathrm{E}\times\mathrm{B}}|$ calculated for the JET ELMy plasmas generally peaks around $R=3.7$ m, outside the range of our fits and close to the range where our values of χ_{eff} become untrustworthy, (2) the plasmas appear to be near marginal stability in the range we consider, so the estimate of $\gamma_{\max}$ is unreliable, and the region further out probably is the region determining the ITG stability of the region we consider.

The arguments given above are sufficiently heuristic that we cannot make conclusions about the applicability of Eq. (5).

C. Alternative dimensionless parameters

In recent flux-tube gyrofluid and gyrokinetic theories based on ITG destabilization, the ion heat transport near marginality can be characterized by a gyro-Bohm expression multiplying a threshold factor

$$\chi_i \propto \rho_i^2 \gamma_{\mathrm{lin}}, \tag{11}$$

with

$$\gamma_{\mathrm{lin}} = (v_{\mathrm{th}}/R)(R/L_{\mathrm{Ti}} - R/L_{\mathrm{crit}}) - \alpha |\omega_{\mathrm{E}\times\mathrm{B}}|, \tag{12}$$

where L_{crit} is the critical value of L_{Ti}, and α is an unknown constant of order unity. This γ_{lin} is similar to the $\gamma_{\max}$ in the previous Section, but with the shearing rate subtracted, lowering the transport. The first term in Eq. (12) gives $\chi_i \propto \chi_{g\mathrm{Bohm}}$. A large reduction of χ_i from $\chi_{g\mathrm{Bohm}}$ would be expected if γ_{lin} is small, and increasing $\omega_{\mathrm{E}\times\mathrm{B}}$ would imply a further reduction.

ITG simulations of a simple ELMy H-mode plasma[36] predict that R/L_{crit} is around 5. The plasma was assumed to have a circular geometry, $T_i = T_e$, $Z_{\mathrm{eff}} = 1$, and adiabatic electrons. The simulations further predict that χ_i should increase rapidly as R/L_{Ti} increases above R/L_{crit}, and should be zero (no anomalous transport) for the linearly stable profiles with R/L_{Ti} below R/L_{crit}. Generally, ITG simulations indicate that L_{crit} has a complicated dependence on plasma conditions. The results from our database show that χ_i tends to increase by a factor of about 2 to 3 in the region $R/L_{\mathrm{Ti}} = 3-6$. The values for $\chi_i/T_i^{1.5}$ increase by an order of magnitude, but that χ_i remains large, with $\chi_i/\chi_{\mathrm{neoclass}} \simeq 10$ even down to R/L_{Ti} as low as 1.

The $|\omega_{\mathrm{E}\times\mathrm{B}}|$ term in Eq. (12) is estimated to be relatively small in the region $0.3<x<0.7$. Furthermore, it shifts the threshold to higher values, the wrong direction to reconcile the observation of large χ_i at low R/L_{Ti}. One theoretical possibility of sustaining active transport dynamics for linearly stable average profiles has been discussed in the context of self-organized criticality (SOC).[37] This indicates that comprehensive nonlinear simulations are needed to investigate whether non-zero initial turbulence could be self-sustained for linearly stable profiles.

There are many alternative sets of dimensionless parameters that could be used in place of Eq. (3). For instance, even though the ratio T_i/T_e deviates by unity by only 30 percent in the region we study, χ_i tends to decrease as the ratio increases. A decrease is expected from ITG theory. Other parameters that vary radially, even though they are approximately constant for each of the plasmas in the dataset, could effect the transport. Examples are q and ε. For instance, we find a good fit for $\chi_i/(\omega_c L_{\mathrm{Ti}}^2)$ using ρ_*, ν_*, A, q, and ε. Again, the ρ_* power is close to the Bohm value.

VII. IMPLICATIONS FOR ITER

The empirical fits for JET ELMy plasmas in Table III can be applied to ITER plasmas. We compare our empirical fit with the χ_{eff} values calculated for two simulations of standard ITER-FDA plasmas yielding a fusion power of P_{DT} of 1.5 GW.[38] One of the simulations has relatively broad plasma profiles and the other has relatively peaked plasma profiles. The electron density peaking, $n_e(0)/\langle n_e \rangle$, are 1.0 and 1.5, respectively. In the range $0.3<x<0.7$, these ITER plasmas have small ρ_* and ν_* and large β compared with the JET plasmas.

We compared the JET empirical fit Eq. (3) to χ_{eff} with those calculated in Ref. 38 For the broad ITER plasma, the empirical fit is lower by a factor of 2 or more, and for the peaked plasma, it is lower by more than a factor of 5. Thus the values of χ_i and χ_{eff} required for the ITER simulations are conservative. Several cautionary notes must be consid-

ered: (1) the reduction of transport with increasing β shown in Fig. 15 is not expected to continue with increasing β; (2) if the Mach number plays an important role, ITER might require considerable current drive to achieve good confinement.

VIII. DISCUSSION

We have derived empirical fits for energy, momentum, and particle conduction coefficients which are generalizations of the empirical fits previously given for $\langle \omega_c \rangle \tau_E$. Our results show that the form of dimensionless parameters in Eq. (3) gives approximate empirical fits to the transport coefficients in quasi-steady state conditions, near the mid-radius. The fits have trends in β and ν_* expected by ITG theory. The scaling in ρ_* lies between the Bohm and gyro-Bohm values.

For the fits in Table III, the transport coefficients and ρ_* are normalized using L_{Ti} as the scale length instead of the minor radius, a, as often used. The choice of L_{Ti} is more appropriate as a local parameter. However, one complication is that L_{Ti} and ρ_i show correlations. Higher performance plasmas have lower L_{Ti} and higher ρ_i. If transport coefficients χ_i, etc. are normalized by $\omega_c a^2$, and ρ_i is normalized by a, regression on our database gives an analogous f_{i}, etc. which differ from those in Table III by having considerably larger ANOVA errors and higher values of the ρ_* power a', close to or above the gyro-Bohm value, (2.6–4.2). The values of b' are even more negative, $-(1.1–1.6)$.

Although we find an approximate fit to the JET results in the form of factored powers in Eq. (3), A considerable variation around the fit remains, as indicated in Fig. 14. Also there remain trends in other dimensionless parameters, such as in the local Mach number, as noted in Sec. VI B. The fits suggest that the factored power form may not be very accurate, with, for instance, deviations at large β, shown in Figs. (15 and 16). The fits also suggest that the variations in A and ν_* are more complicated than that of a simple power.

The scaling of the local $\omega_c \tau_E$ and $\omega_c L_{\mathrm{Ti}}^2/\chi_{\mathrm{eff}}$ are naively expected to have a similar scaling. Our database does not confirm this. The global expressions in Tables I and III do have roughly similar scalings in the parameters ρ_*, and A, but not in β or ν_*. Causes for the differences could be due to: (1) Possible different scaling of the pedestal and core regions, (2) the Monte Carlo methods used in TRANSP gives a more accurate calculation of the fast-ion energy, which must be subtracted to calculate the τ_E, (3) different methods of calculating A are used, and (4) different definitions of the dimensionless parameters, such as ν_* are used.

The empirical fits to the transport coefficients are useful for summarizing results from the JET ELMy H-mode experiments and for extrapolating to other tokamaks. The fits are in approximate agreement with plasmas from the JET identity experiments, which were excluded in the regressions that gave the fits. These include plasmas with I_p as low as 0.8 MA and B as low as 0.8 T. The empirical fit (excluding the toroidal rotation) shows that the values for χ_{eff} computed for ITER-FDR plasmas near the mid-radius, in steady state are rather conservative. The empirical fit is lower than the ITER χ_{eff} by more than a factor of 2.

The JET empirical fits may shed light on the degradation of confinement with increasing density. The ratio $(\chi_i/(\omega_c L_{\mathrm{Ti}}^2))/\rho_*^{2.35}$ tends to decrease with $\bar{n}_e/\bar{n}_{\mathrm{Greenwald}}$, but the empirical fit in Table III does not. Thus variation of transport with $\bar{n}_e/\bar{n}_{\mathrm{Greenwald}}$ appears to be accounted for by the changes in the local dimensionless parameters in Eq. (3).

There are systematic trends for the TRANSP simulations to underpredict the stored energy at low $\langle \beta \rangle$ and to overpredict at high $\langle \beta \rangle$. The transport coefficients have been scaled by the ratio of the TRANSP simulated and magnetically determined energy. Without this renormalization, the empirical fit values change of order 5 percent. For instance, the power of ρ_* shifts slightly further towards the Bohm value.

Several important caveats must be remembered. There are a number of covariances among plasma parameters in the JET experiments. Such covariances make it difficult to isolate causes in the scalings. Also alternative dimensionless parameters such as T_i/T_e can be used to derive good empirical fits. Therefore, our results are an existence proof that dimensionless parameters in the form of Eq. (3) give an approximate fit to the data instead of a strong proof of the specific scalings.

ACKNOWLEDGMENTS

We wish to thank the JET team for providing excellent plasmas and data, to thank G. Hammett and M. Beer for helpful comments, and K. Young for a careful reading of the manuscript. This work was supported in part by the U.S. Department of Energy Contract No. DE-AC02-76CH03073.

APPENDIX: FORMULAS AND UNITS

The thermal energy confinement is defined as

$$\tau_E = W_{\mathrm{th}}/P_{\mathrm{loss}}, \tag{A1}$$

where P_{loss} is the power loss from the thermal plasma via conduction, convection, radiation, and net charge-exchange.

The usual ion and electron heat conductivities are defined by subtracting the particle convection from the thermal heat fluxes

$$q_i \equiv -\chi_i n_i (\partial T_i/\partial r) + \tfrac{3}{2}\Gamma_i q_e \equiv -\chi_i n_e (\partial T_e/\partial r) + \tfrac{3}{2}\Gamma_e. \tag{A2}$$

The effective thermal heat conductions are defined to include both the convective and conductive transport.

$$q_i \equiv -\chi_{i\mathrm{tot}} n_i (\partial T_i/\partial r) q_e \equiv -\chi_{e\mathrm{tot}} n_e (\partial T_e/\partial r). \tag{A3}$$

The one-fluid or effective thermal energy transport coefficient, χ_{eff} is defined from the electron and thermal ion heat fluxes, in analogy with Eq. (A3)

$$q_i + q_e \equiv -\chi_{\mathrm{eff}}[n_i (\partial T_i/\partial r) + n_e (\partial T_e/\partial r)]. \tag{A4}$$

The profile of the isotopic mass of the thermal hydrogenic species is given by

$$A = \frac{(n_{\mathrm{H}} + 2n_{\mathrm{D}} + 3n_{\mathrm{T}})}{(n_{\mathrm{H}} + n_{\mathrm{D}} + n_{\mathrm{T}})}. \tag{A5}$$

The hydrogenic ion gyroradius, ($\propto\sqrt{(T_i/A)}/\omega_c$), is given by

$$\rho_i = 4.7\cdot 10^{-4}\sqrt{(AT_i)}/B[m], \tag{A6}$$

with T_i in keV and the toroidal field B in Tesla. We use $\rho_* = \rho_i / L_{\mathrm{Ti}}$.

The local β is the normalized thermal pressure given by

$$\beta = 9.8\cdot 10^{5}[n_e T_e + n_i T_i]/[8\pi\langle B^2\rangle], \tag{A7}$$

where $\langle B^2\rangle$ is the volume average over the entire plasma of the square of the vacuum toroidal and n_e is in units of $10^{20}/\mathrm{m}^3$. The normalized β_n is given by

$$\beta_n = \langle\beta\rangle/(I_p/(aB)), \tag{A8}$$

where a is the minor radius.

ν_* is the ion collisionality, normalized with the bounce frequency and the toroidal connection length, given by q, the local safety factor times the major radius, R. We use a simple expression, with a constant value for the Coulomb Log

$$\nu_* = 7\cdot 10^{-4}[qRZ_{\mathrm{eff}}n_e]/[\varepsilon^{3/2}T_i^2], \tag{A9}$$

where ε is the local aspect ratio of the minor and major radii, r/R.

[1] F. W. Perkins, D. E. Post, N. A. Uckam, N. Azumi *et al.*, Nucl. Fusion **39**, 2137 (1999).
[2] L. D. Horton, R. Sartori, B. Balet, R. V. Budny *et al.*, Nucl. Fusion **39**, 993 (1999).
[3] M. Keilhacker, A. Gibson, C. Gormezano, P. J. Lomas *et al.*, Nucl. Fusion **39**, 209 (1999).
[4] J. Jacquinot, V. P. Bhatnagar, J. G. Cordey, L. D. Horton *et al.*, Nucl. Fusion **39**, 235 (1999).
[5] J. W. Connor and J. B. Taylor, Nucl. Fusion **17**, 1047 (1977).
[6] B. B Kadomtsev, Fiz. Plazmy **1**, 531 (1975) [Sov. Phys. - J Plasma Phys. **1**, 295 (1975)].
[7] J. G. Cordey, B. Balet, D. V. Bartlett, R. V. Budny *et al.*, Nucl. Fusion **39**, 301 (1999).
[8] P. R. Beavington, *Data Reduction and Error Analysis for the Physical Sciences* (McGraw-Hill, New York, 1969).
[9] J. G. Cordey and the JET Team, Nucl. Fusion **39**, 1763 (1999).
[10] R. V. Budny, J. P. Christiansen, J. G. Cordey, D. R. Ernst, G. Fishpool *et al.*, Plasma Phys. Controlled Fusion **23J**, 1665 (1999).
[11] R. Sartori, D. Borba, R. Budny, G. Conway *et al.*, Contr. Fusion Plasma Phys. **23J**, 197 (1999).
[12] J. P. Christiansen, R. Budny, J. G. Cordey, J. C. Fuchs *et al.*, *Plasma Physics and Controlled Nuclear Fusion Research (Proceedings of the Seventeenth International Atomic Energy Agency Conference on Plasma Physics and Controlled Nuclear Fusion Research 1998* (October 19–24, 1998, Yokohama, Japan) (International Atomic Energy Agency, Vienna, 1998).
[13] L. D. Horton, G. C. Vlases, P. Andrew, V. P. Bhatnagar, A. V. Chankin *et al.*, Nucl. Fusion **39**, 1 (1999).
[14] R. V. Budny, M. G. Bell, H. Biglari, A. C. Janos *et al.*, Nucl. Fusion **35**, 1497 (1995).
[15] B. Balet, D. A. Boyd, D. J. Campbell, C. D. Challis *et al.*, Nucl. Fusion **30**, 2029 (1990).
[16] M. G. von Hellermann and H. Summers, in *Atomic and Plasma Material Interaction Processes in Controlled Thermonuclear Fusion*, edited by Janev (Elsevier, New York, 1993), p. 135.
[17] N. Hawkes and N. Peacock, Rev. Sci. Instrum. **63**, 5164 (1992).
[18] C. Gowers, B. Brown, H. Fajemirokun, P. Nielse *et al.*, Rev. Sci. Instrum. **66**, 471 (1995).
[19] G. Braithwaite, N. Gottardi, G. Magyar, J. O'Rourk *et al.*, Rev. Sci. Instrum. **60**, 2825 (1989).
[20] O. N. Jarvis, J. M. Adams, F. B. Marcus, and G. J. Sadler, Fusion Eng. Des. **34–35**, 59 (1997).
[21] R. V. Budny, M. G. Bell, H. Biglari, M. Bitter *et al.*, Nucl. Fusion **32**, 429 (1992).
[22] D. Borba, B. Alper, R. V. Budny, A. Fasoli *et al.*, Nucl. Fusion **40**, 775 (2000).
[23] J. P. Christiansen and J. G. Cordey, Nucl. Fusion **38**, 1745 (1998).
[24] W. A. Houlberg, K. C. Shang, S. P. Hirshman, and M. C. Zarnstorff, Phys. Plasmas **4**, 3230 (1997).
[25] P. B. Snyder, G. W. Hammett, M. A. Beer, and W. Dorland, *Proceedings of the 26th Conference on Contr. Fusion and Plasma Phys.* ECA **23J** (European Physical Society, Petit-Lancy, 1999), p. 1685.
[26] P. B. Snyder, 1999, Ph.D. Thesis, Princeton University, Dept. of Astrophysics: Gyrofluid Theory and Simulation of Electromagnetic Turbulence and Transport in Tokamak Plasmas.
[27] C. C. Petty and T. C. Luce, Phys. Plasmas **6**, 909 (1999).
[28] G. W. Hammett, M. A. Beer, W. Dorland, S. C. Cowley, and S. A. Smith, Plasma Phys. Controlled Fusion **35**, 973 (1993).
[29] Z. Lin, T. S. Hahm, W. W. Lee, W. M. Tang, and R. B. White, Science **281**, 1835 (1998).
[30] T. S. Hahm, M. A. Beer, Z. Lin, G. W. Hammett *et al.*, Phys. Plasmas **6**, 922 (1999).
[31] Z. Lin, T. S. Hahm, W. W. Lee, W. M. Tang, and P. H. Diamond, Phys. Rev. Lett. **83**, 3645 (1999).
[32] R. D. Sydora, V. K. Decyk, and J. M. Dawson, Plasma Phys. Controlled Fusion **38**, A281 (1996).
[33] T. S. Hahm and K. Burrell, Phys. Plasmas **2**, 1648 (1995).
[34] R. E. Waltz, G. D. Kerbel, and J. Milovich, Phys. Plasmas **1**, 2229 (1994).
[35] D. R. Ernst, M. G. Bell, C. E. Bush, Z. Chang, E. Fredrickson *et al.*, Phys. Plasmas **5**, 665 (1998).
[36] A. M. Dimits, G. Batemann, M. A. Beer, B. I. Cohen *et al.*, Phys. Plasmas **7**, 969 (2000).
[37] P. H. Diamond and T. S. Hahm, Phys. Plasmas **2**, 3640 (1995).
[38] R. V. Budny, D. C. McCune, M. H. Redi, J. Schivell, and R. M. Wieland, Phys. Plasmas **3**, 4583 (1996).